Performance Evaluation of the 32-Module quadHIDAC Small-Animal PET Scanner

Klaus P. Schäfers, PhD[1]; Andrew J. Reader, PhD[2]; Michael Kriens[1]; Christof Knoess[3]; Otmar Schober, PhD, MD[1]; and Michael Schäfers, MD[1]

[1]Department of Nuclear Medicine; University Hospital of Muenster, Muenster, Germany; [2]Department of Instrumentation and Analytical Science, University of Manchester, Manchester, United Kingdom; and [3]Max Planck Institute for Neurological Research; Cologne, Germany

The 32-module quadHIDAC is a commercial, high-resolution animal PET scanner, based on gas multiwire proportional chambers. **Methods:** Several scanner parameters that characterize the performance of the system were evaluated in this study, such as spatial resolution, absolute sensitivity, scatter, and count rate performance. The spatial resolution has been determined with filtered back-projected images of a point source. A line source, a mouse phantom, and a rat phantom have been used to characterize the count rate performance. The scatter fraction and photon absorption have been measured with a mouse scatter phantom. The absolute sensitivity has been determined using a line source with aluminum shields of different thickness. **Results:** Spatial resolution (full width at half maximum) offers values of 1.08, 1.08, and 1.04 mm in the radial, tangential, and axial directions, respectively. The maximum count rate is 370 kcps for a line source of 19 MBq activity. Registration of scattered coincidences is caused primarily by photons scattering in the large coincidence detectors. For a mouse-sized object, only 5% of the measured coincidences scatter inside the animal, whereas 32% of the coincidences scatter inside the detectors. Photon attenuation within a mouse phantom was 22%. After scatter corrections, the absolute sensitivity of the system is 15.2 cps/kBq for a point source and 13.7 cps/kBq for a 7.8-cm-long line source. The peak noise equivalent count rates are 67 kcps@209 kBq/mL for the mouse phantom and 52 kcps@96 kBq/mL for the rat phantom. Finally, a comparison has been made with the microPET R4, a commercial scintillation crystal–based PET camera. **Conclusion:** The results confirm that the quadHIDAC PET scanner, with its large cylindric field of view (165-mm diameter, 280-mm axial length), is particularly suitable for imaging small animals such as mice or rats.

Key Words: animal PET; PET; small-animal imaging; molecular imaging; performance evaluation

J Nucl Med 2005; 46:996–1004

PET is a 3-dimensional imaging technique that has undergone tremendous development during recent years. Noninvasive tracing of molecular pathways in time and space is the key capability of PET, whereby it has become an important tool in the diagnosis of human diseases as well as in biomedical research (*1*).

Small animals such as mice or rats are widely used because of their genetic resemblance to humans, and such models are able to mimic human subjects for both healthy and diseased states (*2*). Applying PET to small animals offers a powerful, noninvasive tool for studying molecular processes in vivo (*3*). Several PET scanners dedicated to animal work have been developed so far with different technical characteristics (*4*).

The 32-module quadHIDAC is a commercially available animal PET scanner that is produced by Oxford Positron Systems (*5*). One of these systems was installed in the University Hospital of Muenster, Department of Nuclear Medicine, in November 2002. The photodetection technique of the quadHIDAC is based on a densely packed array of gas detectors coupled to lead converters, which provide both high 3-dimensional spatial resolution as well as a sufficient level of sensitivity. The scanner has a wide port of 165 mm in diameter and 280 mm in length, offering easy access for various types of animals.

Several performance parameters of the quadHIDAC were evaluated in this study, and a comparison was made with the microPET R4 (Concorde Microsystems; a crystal-based, commercially available animal PET scanner) (*6*). The key aim in this work was to characterize the quadHIDAC's capability for imaging small animals, with a particular emphasis on mice.

MATERIALS AND METHODS

System Description

The quadHIDAC PET scanner uses multiwire proportional chambers (MWPCs) to detect photons originating from positron annihilation. The principle of a MWPC is similar to a Geiger–Mueller counter, in which gas is ionized by an incoming particle or photon. In the quadHIDAC design, however, the ionization is caused by the interaction of photons with lead and the escaping

Received Mar. 15, 2005; revision accepted Apr. 4, 2005.

For correspondence or reprints contact: Klaus P. Schäfers, PhD, Department of Nuclear Medicine, University Hospital of Münster, Albert-Schweitzer-Strasse 33, 48129 Münster, Germany.

E-mail: schafkl@uni-muenster.de

electron is amplified by avalanching, which occurs in the presence of a high electric field. The basic camera design, described by Jeavons et al. (*7*), will be briefly outlined.

Each detector module consists of 3 layers: a converter, a MWPC, and then a further converter (Fig. 1A). Each converter, which converts incoming photons into electrons, contains interleaved lead and insulating sheets, mechanically drilled with a dense matrix of small holes (Fig. 1B). An incoming photon interacts with the lead and causes ionization. An electron that escapes into one of the holes in the converter ionizes the gas, which creates free, thermal electrons. Those electrons are focused to the center of the hole and accelerated toward the MWPC due to a strong electric field applied by a resistor chain to the lead layers. Further avalanching occurs on arrival at the anode wires of the MWPC, where electrons are captured (Fig. 1A). The 2-dimensional (2D) position is located by copper cathode tracks that lie across the surface of each of the 2 converter sections (one converter with tracks in the *x*-direction and one with tracks in the *y*-direction).

The avalanching in the holes together with the focusing effect of the electric field allows a precise 2D localization of the incident photon. A comparison of the cathode track pulse heights (produced from each of the 2 converter sections) allows the original photon interaction point to be localized to 1 of the 2 converters. Eight separate chambers, which are stacked together, provide an excellent depth of interaction information, which maintains the spatial resolution across the field of view (FOV) of the scanner. In fact, very high spatial resolution is the prominent characteristic of the HIgh Density Avalanche Chamber (HIDAC).

Each of the converters has a fine matrix of 0.4-mm diameter holes that have been drilled at a pitch of 0.5 mm. The modules are supplied with argon gas, which is bubbled through a liquid quencher and enriched with diisopropyl ether (an organic hydrocarbon with a high molecular weight: 102) to prevent sparking between the converters and the anode wire plane. Eight modules are stacked together to form one detector bank. The transverse length of a module is increased in accordance with its distance from the center of the FOV, to minimize losses in system sensitivity for particular photon emission trajectories. Four of these detector banks (i.e., 32 modules in total) are attached to a ring gantry that rotates around the FOV. This design results in approximately 15 million single gas detectors being used to cover an active imaging volume of 165 mm in diameter and 280 mm in axial length. All modules are clocked independently with an event dead time of 160 ns.

Data readout is performed at 320 MB/s with a 128-bit bus. The readout interfaces to a dual-processor Pentium personal computer (2 × 1.6 GHz Intel Xeon), which also controls the high voltage for the detector modules. The data acquisition of the detected coincidences is performed "on-the-fly" (event-by- event list-mode data), which offers flexible postprocessing of the data and efficient disk space usage for high spatial sampling. The 4 detector banks rotate back and forth, taking 6 s to cover 180°. The angular position is stored in the list-mode file with a precision of 0.07°. The quadHIDAC has no electronic energy discrimination of the incoming photons, although the photon detection efficiency falls off with decreasing photon energy (*8*)—thus, offering higher detection probability to the 511-keV annihilation photons compared with lower energy scattered photons. This lack of energy discrimination is only a minor problem in small animals such as mice or rats, where little scatter arises from inside the animal. For larger species, such as primates, scatter from inside as well as from outside the FOV will certainly degrade the image quality. A direct measurement of random coincidences is not implemented in the camera design. However, the random coincidence rates are estimated from single count rates and stored in the list-mode data stream. The measurement of transmission scan data for attenuation correction is not implemented.

Image reconstruction can be performed with a standard filtered backprojection (FBP) algorithm as well as with a list-mode expectation maximization (EM) algorithm, such as the one-pass list-mode EM (OPL-EM) method (*9*). The quadHIDAC scanner typically acquires 100–200 million high-precision list-mode events. OPL-EM provides a practical way of reconstructing these coincidence events into a very large image array covering a large FOV. The OPL-EM algorithm, which is based on the standard projection data–based maximum-likelihood expectation maximization (ML-EM) algorithm (*10*), progresses through subsets of the list-mode data, carrying out an image update for each subset. Importantly, the technique includes a model of the point response function of the measurement process, which compensates for resolution-impairing effects such as positron range and finite detector resolution. The reconstruction FOV was restricted to a central subvolume to speed-up reconstruction and to minimize the resulting matrix size. There are 2 key parameters: the number of subsets (which defines the number of coincidence lines used for each image update) and the full width at half maximum (FWHM) of the resolution-modeling kernel.

The air-cooled gantry has a size of 960 mm (width), 710 mm (length), and 990 mm (height) with the gantry port of 165-mm diameter. Part of the electronics is housed in a trolley underneath the gantry within a volume of 1,020 × 730 × 930 mm. The trolley is mounted on 4 wheels to allow easy movement. For standard operation, the quadHIDAC needs no special equipment apart from continuous support of argon gas and diisopropyl ether. A standard

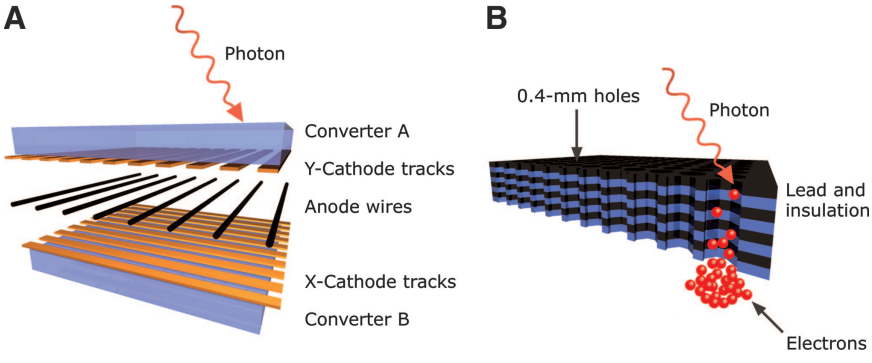

FIGURE 1. (A) Construction of a detector module in 3 layers: 2 converters connected by a MWPC. An incoming photon is converted into an electron that is amplified and accelerated toward the anode wires. (B) Each converter contains interleaved lead and insulation sheets, mechanically drilled with a dense matrix of small holes. A photon interacts with the lead, resulting in an electron that avalanches in a strong electrical field and accelerates toward the MWPC.

bed, which is made of ultralight carbon, is delivered with the camera and can be mounted and unmounted by hand. For exact axial positioning of the bed, a special bed holder with electronic position measurement was constructed by our group, which, in addition, allows easier animal preparation.

Camera Performance

Since there is no overall accepted evaluation standard for animal PET scanners, the performance characteristics were evaluated in accordance with the National Electrical Manufacturers Association (NEMA) NU 2–2001 standards for human PET scanners (*11*). The aim was to simulate the real measurement situation in the best possible way. Due to a failure in one of the 32 modules (module 7 of detector bank 4), all measurements were performed by switching this module off. Therefore, measurements such as sensitivity or absolute count rates are slightly underestimated by 2.9%.

Spatial Resolution. For measurement of the intrinsic spatial resolution, a molecular sieve (0.5-nm pore size, ~2-mm diameter) was soaked with a ^{18}F solution and split into small pieces of ~0.2-mm diameter (*12*). One such point source (~300 kBq ^{18}F), which was not surrounded by a positron annihilator, was mounted on a plastic spike with plasticine, positioned at the center of the gantry and a list-mode acquisition was performed for 30 min. Tomographic images were reconstructed (0.2-mm voxel size) using the OPL-EM algorithm without resolution recovery (using 50 subsets) and FBP using a ramp filter and the Nyquist cutoff frequency. Data were not corrected for randoms, dead time, attenuation, or scatter. The FWHM and full width at tenth maximum (FWTM) in the radial, tangential, and axial directions were calculated by fitting a gaussian function to the reconstructed data and calculating the profile FWHM and FWTM.

Sensitivity. In accordance with the NEMA NU 2–2001 standards (*11*), a line source, filled with ^{18}F water solution, was placed along the central axis of the scanner. Water solution of known radioactivity (^{18}F), which had been measured in a calibrated counter, was used to fill the tube. Therefore, the radioactivity in a syringe was measured before and after filling of a small glass capillary. Five aluminum sleeves with different diameters and wall thicknesses were attached to create different shielding thicknesses of 1.4, 2.7, 4.1, 5.5, and 6.9 mm around the source. A 5-min scan was performed for each shielding thickness. Six experiments were performed with line sources of different length (0.2, 3, 7.8, 15, 20, and 25 cm) to account for the long axial FOV of the quadHIDAC. List-mode data were binned into a set of 2D projections (size, 300 × 160 mm), 15 for each of 64 azimuthal angles (15 polar angles). The "binning ratio" was defined as the ratio of the number of total counts in the projections compared with the number of total counts recorded in the list-mode file. The 64 angles were summed to provide a sufficient count number for the analysis. A set of 15 line profiles was obtained by summing the data of the central 280 mm. For each profile, the position x of the maximum value was determined, and 2 edge points were defined on the profile line at positions (x − 4 mm) and (x + 4 mm) (*13*). Background counts were calculated by interpolating a line between the 2 edge points and summing all counts below the interpolated line together with the counts under the tails of the profile outside the peak. The counts in the peak, taken as the counts above the interpolated line, were summed and divided by the binning ratio to estimate the true coincidences. The total random counts, which are calculated from single events and stored in the list-mode file, were multiplied by the binning ratio and subtracted from the background counts to estimate the scattered coincidences. The number of trues was then plotted as a function of aluminum thickness. The true counts of the unshielded source were calculated by fitting the data to an exponential function using nonlinear regression and then extrapolating the function to the point corresponding to zero shielding (*14*). The sensitivity of the scanner was calculated as the fraction of extrapolated trues compared with the known radioactivity in the corresponding central section.

Count Rate Performance. The count rate performance was measured with 3 different phantoms: (a) an 8-cm-long line source; (b) a 43-mm-diameter, 76-mm-long, water-filled phantom of volume 110 mL (the mouse phantom); and (c) a 60-mm-diameter, 100-mm-long, water-filled phantom of volume 270 mL (the rat phantom). The 8-cm glass capillary, filled with 25 MBq of a ^{18}F solution, was positioned along the axis of the scanner and centered in the FOV. A list-mode acquisition was performed for 6 half-lives of ^{18}F—that is, ~12 h. Each 10-min section of the list-mode data was binned into a set of 2D projections of size 128 × 64 (for 32 azimuthal angles and 15 polar angles). True, random, and scattered coincidences were estimated as described for the sensitivity calculation. The counts stored in each 2D projection for all azimuthal and polar angles were summed to obtain the overall number of coincident events.

The mouse phantom was filled with 30 MBq of a ^{18}F solution and centered in the FOV. Analogous to the line source measurement, a list-mode acquisition was performed for 12 h and list-mode data were binned into 2D projections of size 260 × 170 (for 32 azimuthal angles and 15 polar angles). As before, the "binning ratio" was defined as the ratio of the number of total counts in the projections compared with the number of total counts recorded in the list-mode file. The 32 angles were summed to provide a sufficient count number for the analysis. A set of 15 line profiles was obtained by summing the data of the central slices according to the size of the mouse phantom (76 mm). For each profile, background counts were defined by fitting a squared cosine function to the tails of the activity profile excluding the central area of known object size. The recorded random counts from the list-mode file were subtracted from the background counts to estimate the scattered coincidences. True coincidences were calculated by subtracting background counts from total counts. Measurements of the rat phantom started with an activity of 30 MBq of ^{18}F solution. The data analysis was analogous to that done for the mouse phantom, using the known diameter of the phantom (60 mm) as the scatter boundary.

Noise Equivalent Counts (NECs). The NEC rate function is defined by Strother et al. (*15*):

$$NECR_{Strother} = \frac{T^2}{T + S_{phant} + 2kR}, \qquad \text{Eq. 1}$$

where T and R are the true and random count rates (online random subtraction), S_{phant} is the scatter count rate integrated within the object boundary, and k is the projection fraction. For the quadHIDAC scanner, which normally scans relatively small objects compared with the large scanner FOV, this equation needs to be modified. Since we calculate the scatter coincidences as the counts within the real object, this is independent of the axial FOV length. The parameter k is a correction factor to account for the fact that a phantom is not occupying the whole FOV. For a standard PET scanner, the axial length of the phantom usually exceeds the

scanner's axial extent; therefore, k is simply the ratio of the phantom diameter to the FOV diameter. In the situation of the quadHIDAC, the object of interest is usually much smaller than the FOV. Thus, the extent of the phantom must be accounted for:

$$k = \frac{A_{phant}}{A_{scanner}}, \qquad \text{Eq. 2}$$

where A_{phant} and $A_{scanner}$ are the 2D projected areas of the phantom and the scanner FOV, respectively. The resulting formula for NEC rate calculation is given by:

$$NECR = \frac{T^2}{T + S_{phant} + \left(\frac{A_{phant}}{A_{scanner}}\right) \cdot 2R}. \qquad \text{Eq. 3}$$

Although the quadHIDAC does not subtract randoms online, the factor $2k$ is kept for better comparison with other animal PET scanners. Since k is much smaller than 1 (0.07 for the mouse phantom, 0.13 for the rat phantom), only little differences in NEC rate could be observed between calculation with k and $2k$. NEC rates were calculated for both the mouse phantom and the rat phantom.

Scatter and Attenuation. Due to the large surface and dense material of the detectors, a high scatter fraction is expected. To evaluate the effect of scatter and absorption in a mouse-sized object, a polyethylene phantom (density, 0.95 g/cm^3; 30-mm diameter, 150-mm long) was used, in which a line source can be inserted at a 7-mm distance from the center. A 7.8-cm-long line source was filled with an activity of 9 MBq (^{18}F solution) and 2 list-mode scans (5 min each) were performed with and without applying the scatter phantom (termed "line phantom" and "mouse scatter phantom" in the further analysis). The numbers of true, random, and scattered coincidences were calculated from binned projections as described in the Sensitivity section and normalized to positron decay obtained. The coincidences were divided by the scan length to yield a rate and divided by the computed rate of positron decay. The line source experiment is assumed to produce only scatter in the detectors. By comparing the results with those of the mouse scatter phantom, the percentage of attenuated and scattered coincidences inside a mouse-sized object can be calculated.

Phantom and Animal Studies

A high-resolution phantom was used to assess the resolution capability of the scanner. The phantom consists of a 5-mm-thick polyethylene disk with a diameter of 29 mm, which is divided into 4 sections, each containing holes of different diameters (Fig. 2). The hole diameters are (center-to- center spacing given in parentheses) 0.5 mm (1 mm), 1 mm (2 mm), 1.5 mm (3 mm), and 2 mm (4 mm). The holes were filled with a ^{18}F solution and the phantom was placed in the center of the FOV. An acquisition was performed for 4 h. Data were reconstructed with FBP and with the OPL-EM algorithm, and reconstructed image profiles were obtained in the tangential and axial directions.

In addition to the high-resolution phantom, a small Swiss mouse (22 g) was injected with 10 MBq of ^{18}F-FDG and a 15-min acquisition was performed 1 h after injection. Images were reconstructed using the OPL-EM algorithm. No attenuation or scatter correction were applied to the data. Similarly, a second mouse (27 g) was

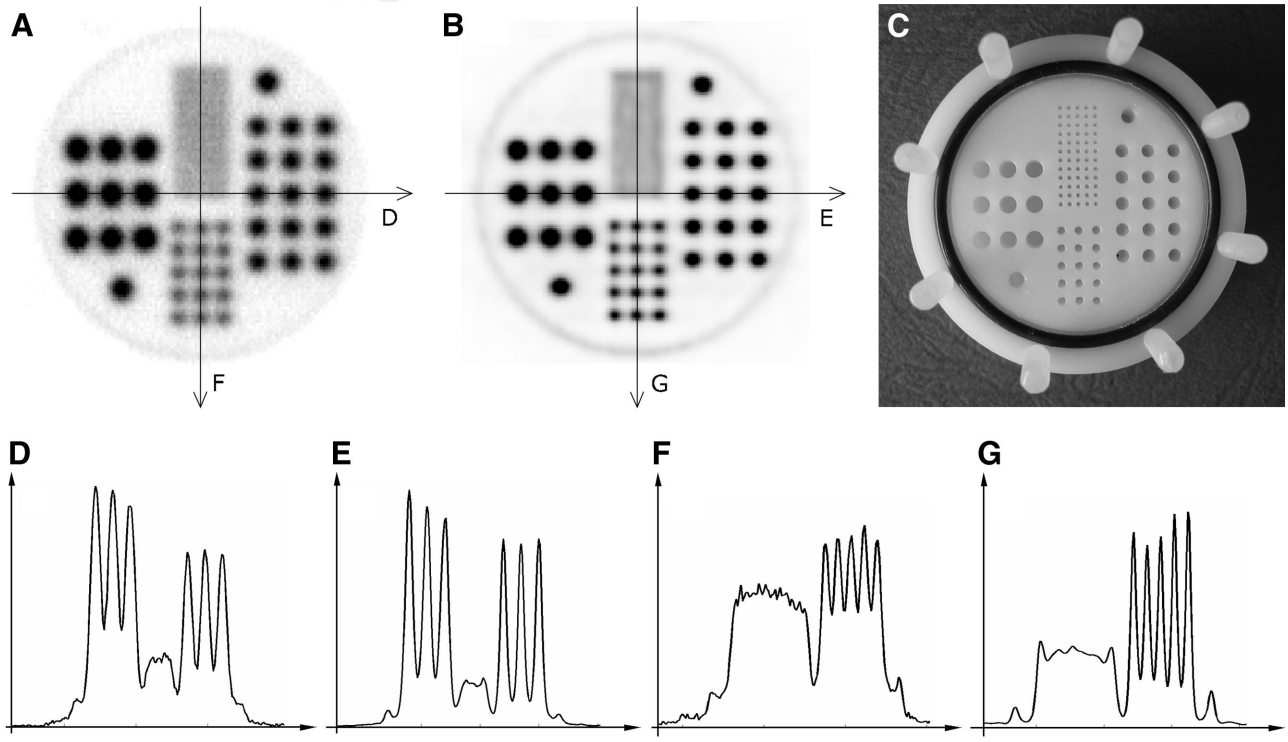

FIGURE 2. Reconstruction results of a ^{18}F-filled high-resolution phantom, constructed from a plastic cylinder, in which holes of different sizes (0.5, 1, 1.5, and 2 mm) were drilled (C). Holes are clearly visible in FBP (A) and OPL-EM (B) reconstructed images down to a size of 1 mm with sharp signals in the profile lines (D and F, horizontal and vertical profiles FBP; E and G, horizontal and vertical profiles OPL-EM).

injected with ^{18}F (12 MBq) and a 15-min list-mode acquisition was performed 1 h after injection. Data were reconstructed as described.

All animals were anesthetized for both the injection and the PET scan acquisitions, which were performed in accordance with the German Laws for Animal Protection.

Comparison of QuadHIDAC and microPET R4

The microPET R4 is a commercial animal PET scanner dedicated to rodent imaging (*6*). Recently, a new commercially available microPET camera has been developed (microPET Focus; Concorde Microsystems) with improved performance characteristics. However, this new camera development is not been included in the comparison, since a published journal article about the performance of the microPET focus was not available at the time of the manuscript preparation. Three figures of merit were used to compare the quadHIDAC with the microPET R4: spatial resolution, absolute sensitivity, and maximum NEC. Due to the entirely different design of each system (particularly the case for the detectors), comparison is not possible with regard to some performance measures (e.g., energy resolution). For the measurement of NECs, the same phantoms (the mouse phantom and rat phantom) were used to ensure comparability of results. The absolute sensitivity of the quadHIDAC is given for both a point source and a 7.8-cm-long line source (analogous to the axial 7.8-cm extent of the microPET). The performance measures of the microPET R4 were published by Knoess et al. (*6*).

RESULTS

Spatial Resolution

The radial, transversal, and axial resolutions for a point source at the center of the FOV are summarized in Table 1. With FBP, radial, tangential, and axial FWHM values are 1.078, 1.081, and 1.038 mm, respectively. Similar spatial resolution values can be achieved with the OPL-EM algorithm, with values of 1.096 mm (radial), 1.082 mm (tangential), and 1.000 mm (radial). The FWHM spatial resolution together with the FWTM values are displayed in Table 1.

Sensitivity

Absolute sensitivity values have been calculated for line sources of different lengths. The scatter-corrected absolute sensitivity for a 0.2-mm point source is 15.2 cps/kBq. Extending the length of the line source, the absolute sensitivity decreases slowly to values of 14.8 cps/kBq (3 cm), 13.7 cps/kBq (7.8 cm), 12.3 cps/kBq (15 cm), 11.2 cps/kBq (20 cm), and 9.6 cps/kBq (25 cm), respectively. Figure 3 displays the absolute sensitivity of the quadHIDAC as a function of the line source length.

TABLE 1
Spatial Resolution (in mm) of quadHIDAC

Spatial resolution at center of FOV	FBP		OPL-EM*	
	FWHM	FWTM	FWHM	FHTM
Radial	1.078	2.411	1.096	2.450
Tangential	1.081	2.416	1.082	2.418
Axial	1.038	2.322	1.000	2.237

*Without resolution recovery.

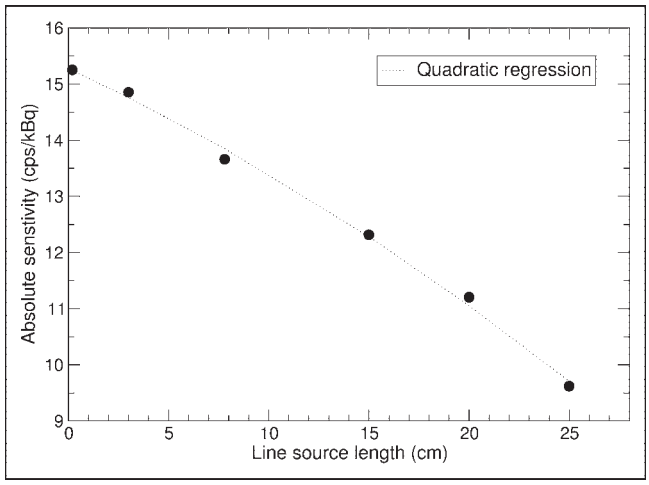

FIGURE 3. Absolute sensitivity of quadHIDAC for different line source lengths. Measurements were performed using method of Bailey et al. (*14*).

Count Rate Performance

Figure 4 shows 3 measurements of the count rate performance of the quadHIDAC, using a line source, the mouse phantom, and the rat phantom. The total coincidence curve saturates at about 370–380 kcps for each of the acquisitions. For a line source, the saturation point is reached at 19 MBq (^{18}F). This rises to 23 MBq and 26 MBq for the mouse phantom and the rat phantom, respectively. The randoms rate at higher activities increases in accordance with the object size—being lower for the line source and greater for the rat phantom. The randoms rate matches the trues rate at an activity of 14 MBq for the mouse phantom and at 11 MBq for the rat phantom. The scattered coincidences are proportional to the "totals-randoms" curve with an average scatter fraction of 32% for the line source, 39% for the mouse phantom, and 46% for the rat phantom.

The NEC rate curves of the mouse phantom and rat phantom, as displayed in Figure 5, seem to follow a quadratic curve with respect to the activity inside the FOV; however, points spread, especially at higher count rates, due to statistical variances of the background-fitting method. The measured maxima are 67 kcps@23 MBq (67 kcps@209 kBq/mL) for the mouse phantom and 52 kcps@26 MBq (52 kcps@96 kBq/mL) for the rat phantom.

Scatter and Attenuation

Table 2 summarizes the analysis of scatter and attenuation in a mouse-sized object. "Total" is the coincidences rate in the projection divided by the calculated positron decay rate. "Trues" is the normalized coincidences rate of the signal peak—thus, the trues rate. A value of 0.0149 was calculated for the line source and 0.0115 was calculated for the mouse scatter phantom. "Scatter" comprises the scattered coincidence rate (without the randoms). The scatter

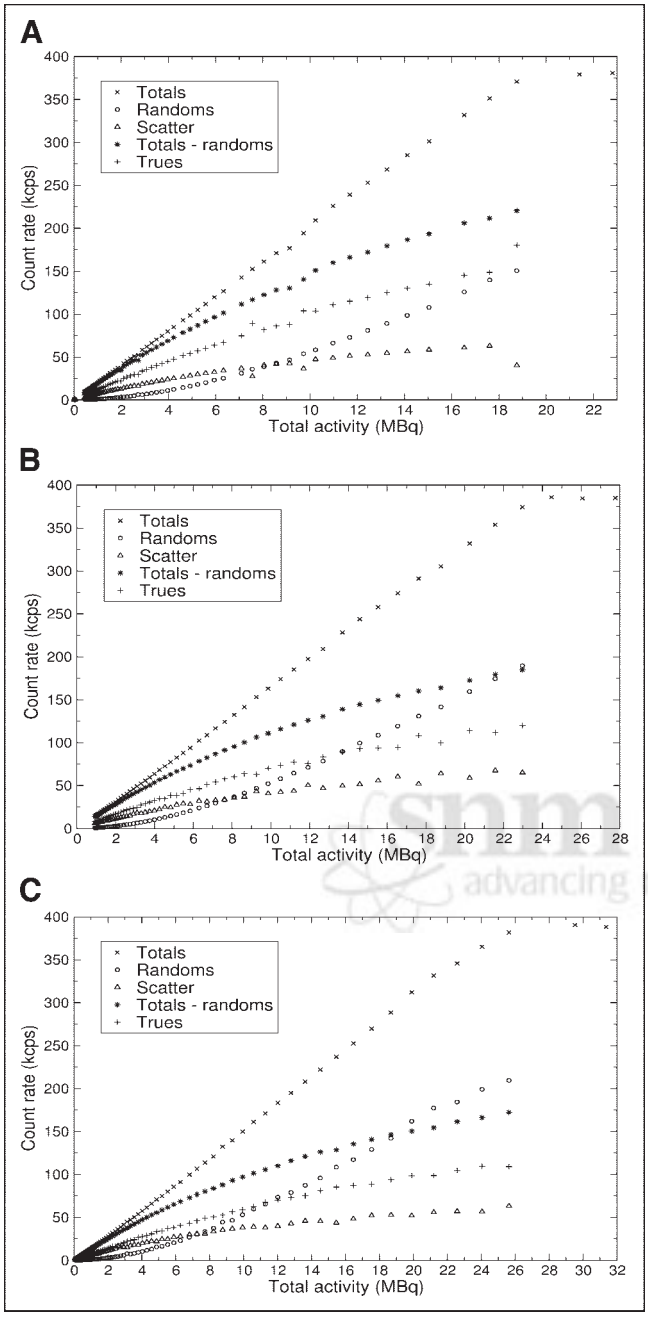

FIGURE 4. Count rate performance measured with line source (A), mouse phantom (B), and rat phantom (C). Denoted by × is the rate of the total number of detected coincidences. Subtracting randoms (denoted by ○), estimated from the single rate yields the set of stars (*). True unscattered coincidence rate (denoted by +) was obtained by subtracting scattered events (△).

fraction, which is the scatter divided by the total, is enhanced from 32% to 37% by adding scattering material to the line source, which indicates that 5% of the coincidences scatter inside the mouse. By comparing the numbers of signal counts from the mouse scatter phantom with those from the line source, a fraction of 22% can be calculated, which is the coincidences absorbed inside the mouse.

Phantom and Animal Studies

The reconstructed images of a high-resolution phantom are displayed in Figure 2. The holes are clearly visible down to a diameter of 1 mm. Only the smallest holes (0.5 mm) are beyond the resolution capability of the quadHIDAC at this level of acquisition statistics. It has been shown before that the spatial resolution is uniform within the entire axial and transaxial FOV (*7*). This is also demonstrated in Figure 2, where no resolution degradation is observed toward the edge of the phantom. The OPL-EM images (Fig. 2B) show higher contrast compared with FBP reconstructed images (Fig. 2A), which is reflected in sharper signal profiles with lower background levels.

Figures 6A and 6B show coronal images of a mouse, where the data were acquired 1 h after injection of 10 MBq of ^{18}F-FDG. Figure 6A is a maximum-intensity-projection image that demonstrates the capability of the scanner to detect even the smallest structures such as the heart or the kidneys of a small mouse. Figure 6B is one coronal slice through the center of the heart, which again shows the high spatial resolution, allowing the heart to be viewed in detail. Even the right ventricle of the heart (which has a submillimeter wall thickness) is clearly visible. The image of a second mouse, injected with 12 MBq of ^{18}F, is shown in Figure 6C. Again, very small bone and rib structures are visible.

Comparison of quadHIDAC and microPET R4

Table 3 gives a comparison of the quadHIDAC and the microPET R4. As anticipated, the spatial resolution of the quadHIDAC is its major strength. A volumetric spatial resolution of 1.2 μL within the whole FOV can be achieved with FBP reconstruction. The microPET R4 has its highest spatial resolution in the center of the FOV (5.1 μL) using a 350- to 650-keV energy window (these energy levels were used for all comparisons). However, resolution degrades with increasing radial distance from the center of the FOV, which is due to the lack of depth of interaction information. At a radial position of 10 mm, a value of 15.6 μL has been

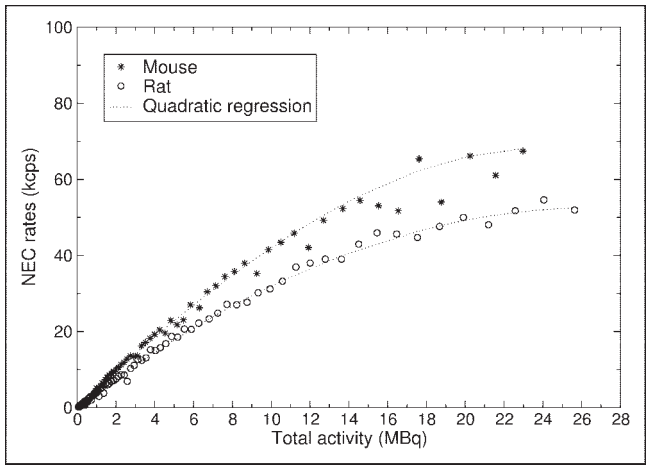

FIGURE 5. NEC rates for mouse phantom and rat phantom.

TABLE 2
Count Rate Measurements of Line Source and Mouse Phantom Experiment Normalized to Computed Coincidence Decay Rate

Parameter	Total	Trues	Scatter	Scatter fraction (%)	Attenuation fraction (%)
Line source	0.0238	0.0149	0.0076	32	—
Mouse scatter phantom	0.0203	0.0115	0.0075	37	22

measured. The absolute sensitivities of both scanners are comparable. The scatter-corrected sensitivity for a 7.8-cm line source (the axial FOV length of the microPET R4) is 13.7 cps/kBq for the quadHIDAC compared with 12.2 cps/kBq for the microPET R4 using a 350- to 650-keV energy window. The maximum NEC rate (mouse phantom) of the microPET R4 is 168 kcps@824 kBq/mL, whereas the quadHIDAC has a maximum at 67 kcps@209 kBq/mL (Fig. 5). For the rat phantom, the maximum values are 52 kcps@96 kBq/mL (quadHIDAC; Fig. 5) and 89 kcps@298 kBq/mL (microPET R4).

DISCUSSION

The aim of this work was to evaluate the performance parameters of the 32-module quadHIDAC PET scanner, an improved version of a previously assessed 16-module quadHIDAC (*7*). In doubling the number of detector modules from 16 to 32, a higher absolute sensitivity of 15.2 cps/kBq for a point source is obtained, compared with 8.9 cps/kBq (point source) for the 16-module quadHIDAC (*7*). The sensitivity enhancement is related to 2 opposite effects. First, the sensitivity is a function of the squares of detection efficiency, which has an inverse exponential dependence on lead thickness, which is directly related to the number of modules. Second, the outer modules do not cover the same acceptance angle in the axial direction and, therefore, the sensitivity, which is linear to the acceptance angle, is reduced. For longer objects, the absolute sensitivity is degrading slowly down to a value of 9.6 cps/kBq for a 25-cm-long object. This is a major advantage of the camera design over crystal-based cameras, since larger animals can be scanned at once without moving the bed. The significant improvement in sensitivity compared with the 16-module version will of course be of benefit in the investigation of metabolic processes in small animals.

Dead time has not been incorporated in the present work. An approach based on the estimation from single events, as described (*16*), was found to underestimate the real contribution, especially at higher count rates. A proper dead-time estimation method must be developed in further investigations.

The calculation of true and scattered coincidences presented in this article depends primarily on the choice of the background distribution model. Several different empiric approaches for the background distribution within the object—for example, a flat function, a gaussian function, a

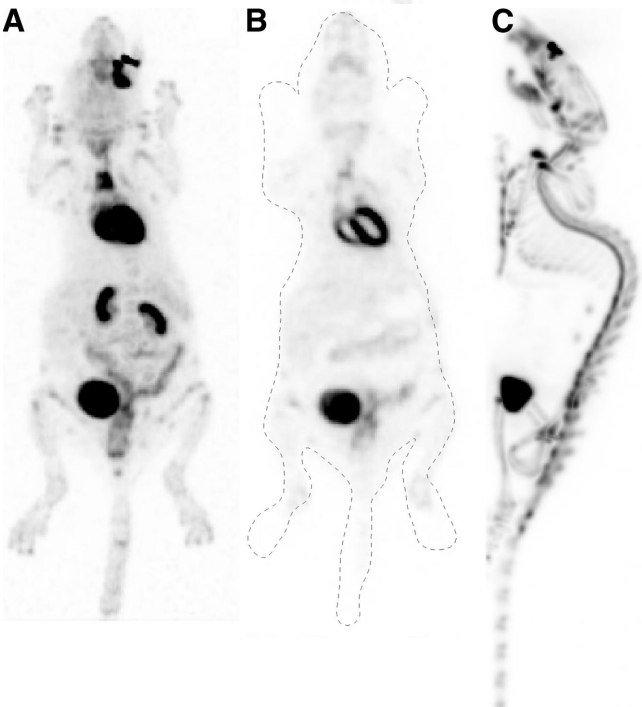

FIGURE 6. (A and B) Images (OPL-EM) of 22-g mouse, acquired in 15 min, 1 h after injection of ^{18}F-FDG show maximum intensity projection (A) and a single central slice (B). (C) Maximum intensity projection of 27-g mouse, 1 h after injection of ^{18}F fluoride.

TABLE 3
Comparison of quadHIDAC and microPET R4

Parameter	quadHIDAC	microPET R4
Volumetric spatial resolution (μL)		
Center of FOV	1.2	5.1
Sensitivity (cps/kBq)		
Line source	13.7*	12.2†
Point source	15.2	24.5†
Maximum NEC rate		
Mouse phantom	67 kcps@209 kBq/mL	168 kcps@824 kBq/mL†
Rat phantom	52 kcps@96 kBq/mL	89 kcps@298 kBq/mL†

*Calculated for 7.8-cm line source.
†Energy threshold, 350–650 keV.
Data for comparison are from (*6*).

cosine, and a squared cosine function—were investigated for different object sizes. It was found that a squared cosine function followed most likely the anticipated background distribution in the mouse phantom and rat phantom, whereas all other approaches seemed to underestimate the true contribution. The exact distribution of the scatter background which comprises both the scatter distribution inside the detectors as well as scatter in the objects is still unknown. This has to be investigated in further studies which will involve simulations of the detector physics.

Spatial resolution is consistently good, with average values (FWHM) of 1.07 mm. These high levels of resolution arise from the high packing fraction of the holes within the converters and the depth of interaction information. The spatial resolution of the quadHIDAC is almost uniform within the entire FOV (*16*), which allows the investigation of larger animals in a single experiment without degradation of the spatial resolution toward the edges of the FOV. Slightly higher resolution values were obtained in the axial direction compared with the transaxial direction. This may have to do with an inaccuracy of the center of rotation during the camera turn. The same effect has been reported by Missimer et al., with values of 1.10 mm in the axial direction (at the center of the FOV) and 1.18 in the transaxial direction (*16*). Further comparisons of resolution measurements obtained without rotating the camera are needed to prove this hypothesis. The high-resolution phantom demonstrated that the spatial resolution does not degrade toward the edges of the phantom, which is in contrast to similar measurements with the microPET R4 scanner (*6*).

Image reconstruction with the quadHIDAC is a time-consuming process when using submillimeter pixels and large reconstructed data arrays. For instance, the OPL-EM reconstruction of a 25-g mouse (reconstructed size, 110 × 60 mm; 0.4-mm pixels) takes about 2 h for a standard ^{18}F-FDG acquisition (10 MBq injected, 15-min acquisition, 1 h after injection). This needs to be investigated and faster algorithms must be developed to speed up the postacquisition processing. Using a high-end computer system, OPL-EM offers a reasonably fast approach to reconstruction, which also avoids losses in resolution that can arise from binning the data into sinograms. Attenuation, random, dead-time, and scatter corrections are not yet applied to the data within the reconstruction process. The low scatter fraction in a mouse is a minor problem and is not noticeable in any image degradation (Fig. 6) but certainly becomes more important for larger species, where scatter within the animal contributes more significantly to regions of interest within the reconstructed image. From a quantitative point of view, of course, these corrections still need to be performed. The OPL-EM algorithm has been adapted recently to integrate corrections for scatter and absorption (*17*). However, the absence of hardware energy discrimination and attenuation measurements inhibit a simple solution to the problem. A simulation and modeling of the complex detector physics is needed to develop new reconstruction algorithms.

With MWPCs electrical breakdowns can occur, which are compensated for by switching off the high voltage for a short time (about 60 s). This, in turn, leads to a gap in data acquisition. An electrical breakdown may occur randomly and without warning within an experiment. A correction for count losses has to be incorporated into the reconstruction process, and the scanner hardware has to ensure that such count losses are negligible. One module (module 7 of detector 4) had to be switched off during the measurements because of a technical failure. The effect on the total amount of detected coincidences is a count rate reduction of 2.9%. This has been quantified with a point source by measuring the total coincidence rate while switching off all modules successively. The contribution of each module to the number of coincidences is (module numbers from module position outside to inside) as follows: module 8, 2.6%; module 7, 2.9%; module 6, 3.4%; module 5, 3.7%; module 4, 4.1%; module 3, 3.7%; module 2, 3.3%; and module 1, 1.3%.

In comparison to the microPET R4, the quadHIDAC is competitive in terms of sensitivity and spatial resolution. The absolute sensitivity of the central 7.8-cm FOV (13.7 cps/kBq) is virtually the same as that for the microPET R4 (12.2 cps/kBq). However, the strength of the quadHIDAC is its ability to scan an animal in a single acquisition without moving the bed. The high fraction of scatter that originates in the detectors is a main limitation of the quadHIDAC. This is reflected in significantly lower NEC rates in the "mouse phantom" compared with the microPET R4 (67 kcps@209 kBq/mL vs. 168 kcps@824 kBq/mL). For larger animals ("rat phantom") the NEC peak values are similar between quadHIDAC and microPET (52 kcps@96 kBq/mL vs. 89 kcps@298 kBq/mL). However, the activity concentrations at the NEC peak values are much lower compared with the microPET R4. Tracers with high specific radioactivity are essential to use the full capacity of the quadHIDAC. Overall, the quadHIDAC is very stable and reliable. Within 1 y, 800 single scans have been performed in our laboratory.

CONCLUSION

The quadHIDAC is a dedicated animal PET scanner with very high spatial resolution, uniform within a large FOV (280-mm axial length, 165-mm diameter). The high spatial and temporal resolution together with a good absolute sensitivity make the scanner a powerful tool for researchers in biomedical science and the pharmaceutical industry.

ACKNOWLEDGMENTS

We gratefully acknowledge Dr. Alan Jeavons for his suggestions concerning the performance measurements as well as useful discussions, Christine Bätza for her help in data acquisition and preparing the mouse images, and Dr. Marilyn Law for her help in preparing the manuscript.

REFERENCES

1. Phelps ME. Molecular imaging with positron emission tomography. *Nat Med.* 2002;52:303–342.

2. Paigen K. A miracle enough: the power of mice. *Nat Med.* 1995;1:215–220.
3. Myers R, Hume S, Bloomfield P, et al. Radio-imaging in small animals. *Psychopharmacology.* 1999;13:352–357.
4. Schäfers KP. Imaging small animals with positron emission tomography. *Nuklearmedizin.* 2003;42:86–89.
5. Jeavons A. The quadHIDAC. Available at: http://www.oxpos.co.uk. Accessed July 26, 2004.
6. Knoess C, Siegel S, Smith A, et al. Performance evaluation of the microPET R4 PET scanner for rodents. *Eur J Nucl Med.* 2003;30:737–747.
7. Jeavons AP, Chandler RA, Dettmar CAR. A 3D HIDAC-PET camera with sub-millimetre resolution for imaging small animals. *IEEE Trans Nucl Sci.* 1999;46:468–473.
8. Jeavons A, Hood K, Herlin G, et al. The high-density avalanche chamber for positron emission tomography. *IEEE Trans Nucl Sci.* 1983;30:640–645.
9. Reader AJ, Ally S, Bakatselos F, et al. One-pass list-mode EM algorithm for high resolution 3D PET image reconstruction into large arrays. *IEEE Trans Nucl Sci.* 2002;49:693–699.
10. Shepp LA, Vardi Y. Maximum likelihood reconstruction for emission tomography. *IEEE Trans Med Imaging.* 1982;1:113–122.
11. National Electrical Manufacturers Association. *NEMA Standards Publication NU 2-2001: Performance Measurements of Positron Emission Tomography.* Rosslyn, VA: National Electrical Manufactures Association; 2001:1–45.
12. Bailey DL, Snowdon G, Cooper RG, et al. The use of molecular sieves to produce point sources of radioactivity. *Phys Med Biol.* 2004;49:N21–N29.
13. Guzzardi R, Bellina CR, Jordan K, et al. Methodologies for performance evaluation of positron emission tomographs. *J Nucl Biol Med.* 1991;35:141–151.
14. Bailey DL, Jones T, Spinks TJ. A method for measuring the absolute sensitivity of positron emission tomographic scanners. *Eur J Nucl Med.* 1991;18:374–379.
15. Strother SC, Casey ME, Hoffmann EJ. Measuring PET scanner sensitivity: relating count rates to image signal-to-noise ratios using noise equivalent counts. *IEEE Trans Nucl Sci.* 1990;37:783–788.
16. Missimer J, Maid Z, Honer M, et al. Performance evaluation of the 16-module quad-HIDAC small animal PET camera. *Phys Med Biol.* 2004;49:2069–2081.
17. Manavaki R, Reader AJ, Keller C, et al. Scatter modelling for 3D PET list-mode EM reconstruction [abstract]. *IEEE Nuclear Science Symposium and Medical Imaging Conference*; November 10–16, 2002; Norfolk, Virginia; Conference Record: M13-2.